ADVANCED HEALTHCARE MATERIALS
www.advhealthmat.de

Optimizing Bifurcated Channels within an Anisotropic Scaffold for Engineering Vascularized Oriented Tissues

Yongcong Fang, Liliang Ouyang, Ting Zhang, Chengjin Wang, Bingchuan Lu, and Wei Sun*

Despite progress in engineering both vascularized tissues and oriented tissues, the fabrication of 3D vascularized oriented tissues remains a challenge due to an inability to successfully integrate vascular and anisotropic structures that can support mass transfer and guide cell alignment, respectively. More importantly, there is a lack of an effective approach to guiding the scaffold design bearing both structural features. Here, an approach is presented to optimize the bifurcated channels within an anisotropic scaffold based on oxygen transport simulation and biological experiments. The oxygen transport simulation is performed using the experimentally measured effective oxygen diffusion coefficient and hydraulic permeability of the anisotropic scaffolds, which are also seeded with muscle precursor cells and cultured in a custom-made perfusion bioreactor. Symmetric bifurcation model is used as fractal unit to design the channel network based on biomimetic principles. The bifurcation level of channel network is further optimized based on the oxygen transport simulation, which is then validated by DNA quantification assay and pimonidazole immunostaining. This study provides a practical guide to optimizing bifurcated channels in anisotropic scaffolds for oriented tissue engineering.

Dr. Y. Fang, Prof. T. Zhang, C. Wang, B. Lu, Prof. W. Sun
Biomanufacturing Center
Department of Mechanical Engineering
Tsinghua University
Beijing 100084, P. R. China
E-mail: t-zhang@tsinghua.edu.cn
Dr. Y. Fang, Prof. T. Zhang, C. Wang, B. Lu, Prof. W. Sun
Biomanufacturing and Rapid Forming Technology Key Laboratory of Beijing
Beijing 100084, P. R. China
Dr. Y. Fang, Prof. T. Zhang, C. Wang, B. Lu, Prof. W. Sun
"Biomanufacturing and Engineering Living Systems" Innovation International Talents Base (111 Base)
Beijing 100084, P. R. China
Dr. L. Ouyang
Department of Materials
Imperial College London
London, SW7 2AZ, UK
Prof. W. Sun
Department of Mechanical Engineering
Drexel University
Philadelphia, PA 19104, USA

The ORCID identification number(s) for the author(s) of this article can be found under https://doi.org/10.1002/adhm.202000782

DOI: 10.1002/adhm.202000782

Cell alignment and spatial orientation of extracellular matrix (ECM) are widely found in oriented tissues including heart, tendon, nerve, and muscle tissues (**Figure 1**A).[1] Such structural anisotropy affects the mechanical properties of tissues and modulates cellular activities including cytoskeleton reorganization, integrin activation, and ECM remodeling.[2] Therefore, developing scaffold that can guide cell alignment and organization would be highly beneficial for the regeneration and maturation of functional oriented tissues. Different scaffolds with anisotropic structures have been explored to guide in vitro cell alignment by exploiting nanotopographical patterns such as oriented electrospun fibers, ridges, and grooves; however, such strategy has often been restricted to 2D scaffolds or thin films.[3] Moreover, the compact fibrous structures within electrospun scaffolds were found to inhibit cell infiltration into the scaffold and result in deficient tissue regeneration.[4] These considerations have led to the fabrication of 3D scaffolds with well-defined microscale structural patterns, such as oriented micropores and accordion-like honeycombs, in order to control cell alignment and organization in the 3D environment.[5]

However, owing to the lack of vascularization, it is still a great challenge to engineer 3D thick oriented tissues for skeletal muscle and cardiac regeneration and other biomedical applications.[6] Because of the limited diffusion distance of oxygen and nutrients (≈100 µm), perfusable channel networks that can support endothelium formation are often a prerequisite for mass transfer inside the scaffold.[7] Therefore, to achieve vascularized oriented tissue regeneration, there is an urgent need to develop a 3D scaffold that integrates vascular channels with anisotropic structures. Although the general demand for vascularization has evoked massive efforts focused on constructing perfusable channels within cell-laden hydrogels or acellular scaffolds,[8] minimal work has been done with anisotropic scaffolds for thick oriented tissue engineering.[9] Moreover, an effective approach to designing and optimizing the channels within anisotropic scaffolds is currently lacking. The anisotropic structure and induced spatial cell alignment would undoubtedly have a significant effect on oxygen and nutrient delivery, which has hindered the direct use of well-studied optimizing approaches based on isotropic scaffolds.[10]

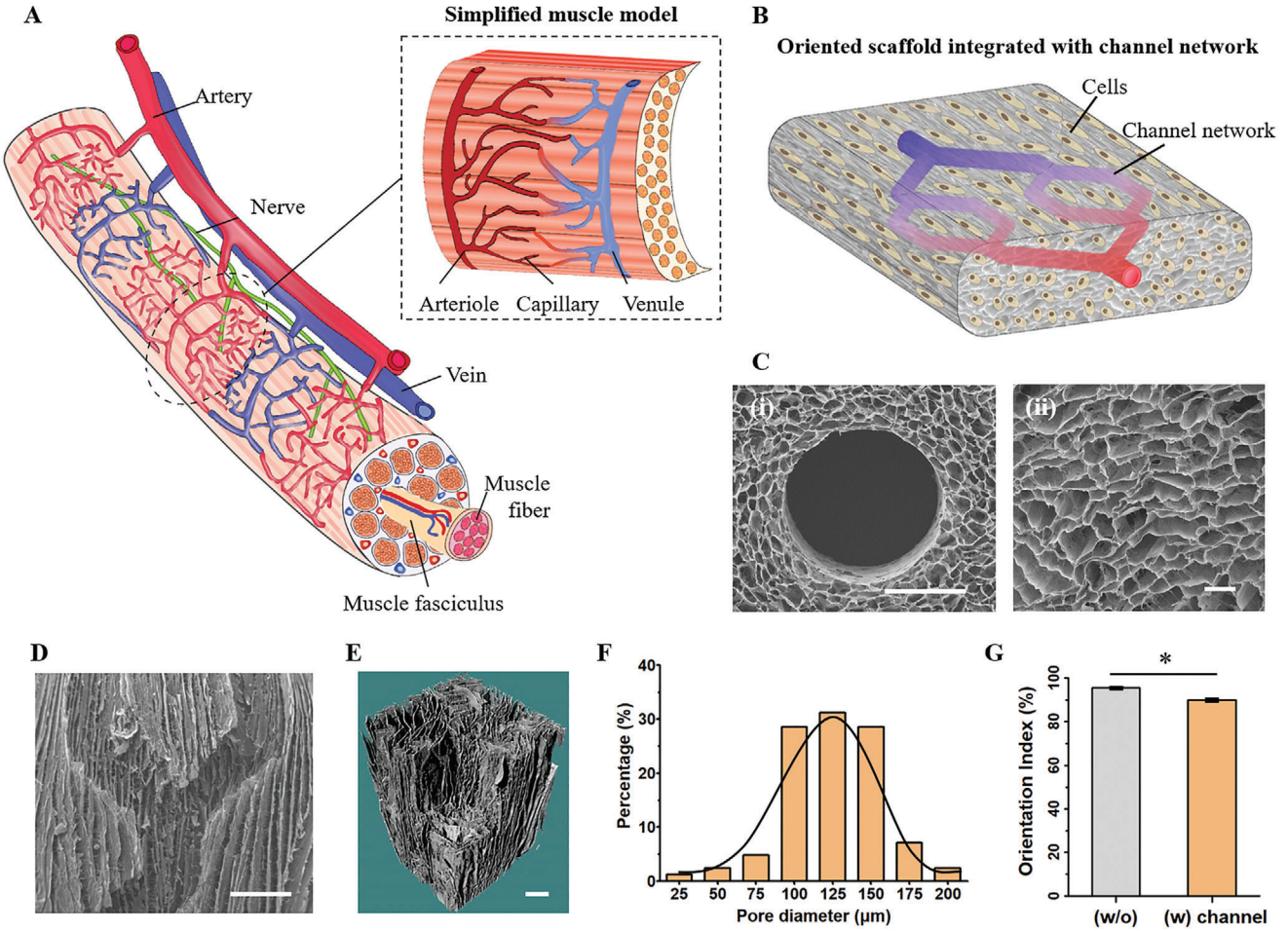

Figure 1. Schematic design, morphology, and characterization of the anisotropic scaffold. A) Schematic illustration of the native skeletal tissue with hierarchical vasculature. B) Schematic design of the biomimetic scaffold integrated with oriented micropores and channel networks for oriented tissue engineering. C) Cross-section SEM image of fabricated scaffold sections near the channels (i, scale bar: 500 μm) and magnified image of micropores (ii, scale bar: 100 μm). D) Longitudinal SEM image of fabricated scaffold sections (scale bar: 500 μm). E) The reconstructed fabricated scaffold 3D model from μCT images (scale bar: 200 μm). F) The diameter ranges of micropores within the fabricated scaffold. G) The oriented index of fabricated scaffolds with/without channels. Student's *t*-test was used to analyze the data, $*p < 0.05$.

To address this challenge, here we propose an approach to design and optimize the channel network in a cell-seeded anisotropic scaffold based on oxygen transport simulation and biological experiments. The channel network governed by biomimetic principles were designed by using a symmetric bifurcation model as a fractal unit. Based on the oxygen transport simulation, the bifurcation level of channel network was further optimized to improve oxygen transport efficiency. The oxygen transport simulation results were validated by pimonidazole immunostaining and DNA quantification assay with muscle precursor (C2C12) cells seeded and cultured in a custom-made perfusion bioreactor. This numerical model-based strategy could be employed as a promising candidate to design vascular channels within oriented tissues/organs, which would accelerate the development and application of vascularized oriented tissues.

We first fabricate oriented porous scaffold with an integrated channel network via a templating method and unidirectional freeze-drying technique as previously reported (Figure 1B and Figure S1, Supporting Information).[9] Generally, the sacrificial template should be capable of rapid dissolution in an aqueous solution without affecting the cells and have good mechanical properties for handling and transfer.[11] Furthermore, the sacrificial template must be able to endure the freeze-drying process as this is a prerequisite for anisotropic scaffold fabrication. Based on these requirements, polyvinyl alcohol (PVA) was chosen as a template material for its favorable physiochemical properties. The bifurcated PVA structures were successfully constructed with customized geometry using a micromolding technique. The multilevel bifurcated template preserved a gradually decreasing diameter along the branching direction, with a diameter of ≈1000 μm at bifurcation level 0 and ≈400 μm at bifurcation level 3 (Figure S2A,B, Supporting Information). After sequential casting, freeze-drying and crosslinking of a chitosan/collagen hybrid material, the channel network was generated by immersing the scaffold in deionized water overnight to dissolve the sacrificial template (Figure S2C, Supporting Information). The bifurcated channels presented a standard circular cross-section within a highly aligned porous scaffold (Figure 1C,D). The resulting

channel was marginally smaller than the template, with a less than 10% difference in diameter for all bifurcation levels that was likely due to scaffold shrinkage in water (Figure S2D, Supporting Information). Nevertheless, the shape and size of the fabricated channel network closely resembled that of the sacrificial template.

It should be noted that the sacrificial template was precoated with a thin layer of poly(D,L-lactide-*co*-glycolide) (PLGA) to prevent it from dissolving during the chitosan/collagen solution casting and freezing process. As a result, a thin, O_2/CO_2 permeable polymer membrane remained on the inner walls of the channels. To modulate membrane permeability to small molecules and proteins, we introduced micropores (10–50 μm) to the membrane using porogen leaching (Figure S3, Supporting Information). In addition, the channel surface (i.e., the polymer membrane) was coated with collagen to improve endothelial cell adhesion and growth. This polymer layer served as a seeding substrate for endothelial cells and a potential biomimetic basement membrane. We illustrated this by seeding human umbilical vein endothelial cells (HUVECs) into the channel networks by perfusion through a syringe pump (Figure S4A, Supporting Information). After perfusion culture for 3 d, the majority of the HUVECs adhered and spread on the channel surface, revealed by the staining of F-actin and cluster of differentiation 31 (CD31) proteins (Figure S4B–G, Supporting Information). The endothelial cells continuously proliferated and organized into a more confluent monolayer lining the channel surface on day 7 (Figure S4H, Supporting Information). As suggested by our previous study, cell migration and sprouting through the wall is possible due to the embedded microholes in the membrane.[9] It should also be noted that endothelialization efficiency is highly subject to the cell density, seeding techniques, and polymer biocompatibility.[12]

Oriented micropores with diameters ranging from 50 to 150 μm were observed within the scaffold using microcomputed tomography (μCT) reconstruction and scanning electron microscopy (SEM) imaging (Figure 1E,F). Oriented micropores formed after the sublimation of oriented solvent crystals, which were induced under a unidirectional thermal gradient. The applied ice crystal templating approach is advantageous in regulating scaffold pore sizes in favor of cell infiltration and metabolic delivery.[13] After channel introduction, the oriented degree of the micropores decreased slightly but remained high (90.0% ± 1.6%) throughout the entire scaffold (Figure 1G). These results demonstrated that scaffold structural anisotropy could be preserved by selecting suitable material and geometrical design for sacrificial templates to minimize interference on the unidirectional temperature field.

Oriented micropore-guided C2C12 cell alignment was demonstrated by F-actin staining (**Figure 2**A,B). After 3 d of perfusion culture, C2C12 cells presented a highly anisotropic alignment. The orientation angle distributions of the cells and micropores were highly overlapped (Figure 2C,D), which suggested that cell elongation and alignment were mainly regulated by the oriented micropores within the scaffold. The results were consistent with our previous work in which oriented porous scaffolds could guide cardiomyocyte orientation.[9] Cell elongation and alignment are essential for tissue formation and maturation of muscles and other oriented tissues. The oriented micropores also modulated the mechanical properties (Figure 2E). The elastic modulus parallel to the oriented micropores (Ani_L) was 82.0 ± 13.5 kPa, significantly higher than that vertical to the oriented micropores (Ani_V; 27.3 ± 8.9 kPa). In contrast, the isotropic porous scaffold (Iso) possessed an elastic modulus (38.5 ± 8.3 kPa) between those of Ani_L and Ani_V. Interestingly, the introduction of channel networks (Ani_C) led to a higher elastic modulus (169.0 ± 67.5 kPa) when compared to its channel network-free counterpart (Ani_L). This indicates that rational channel design is necessary to tailor the mechanical properties and maintain the structural anisotropy of the scaffold. It is widely recognized that biomechanical scaffold and substrate properties influence the morphogenesis, differentiation, and functional maturation of different cells including muscle cells and cardiomyocytes.[14] Scaffold mechanical properties should be tailored to match that of specific native ECM for the functional regeneration and maturation of oriented tissues.[15] For example, the elastic modulus of adult human myocardium is reportedly 10–20 kPa, whereas those for skeletal muscle and cartilage are around 10 and 500 kPa, respectively.[16] Further design iterations could yield an anisotropic scaffold with mechanical properties tailored for specific oriented tissues by tuning the collagen/chitosan formulation and temperature gradient as reported in our previous work.[9]

Owing to the anisotropic scaffold structure and induced spatial cell alignment, oxygen and nutrient delivery within an anisotropic scaffold is very distinct from those in an isotropic scaffold. The effective oxygen diffusion coefficient and hydraulic permeability are two key parameters that determine the mass transport properties of a scaffold.[17] Given this, we first measured these two parameters of acellular scaffolds using a customized experimental setup. For oriented porous scaffolds, the effective oxygen diffusion coefficient at the Ani_L direction was $(1.5 \pm 0.2) \times 10^{-5}$ cm^2 s^{-1}, much higher than that at the Ani_V direction ($(2.3 \pm 0.6) \times 10^{-6}$ cm^2 s^{-1}). As a control, the isotropic porous scaffold had an effective oxygen diffusion coefficient between the above two oriented scaffold values ($(6.2 \pm 0.4) \times 10^{-6}$ cm^2 s^{-1}; Figure 2F,G). For oriented porous scaffolds, the hydraulic permeability at the Ani_L direction was much higher than that at the Ani_V direction ($(5.1 \pm 0.3) \times 10^{-12}$ m^2 and $(1.2 \pm 0.2) \times 10^{-12}$ m^2, respectively). Similarly, the isotropic porous scaffold had a hydraulic permeability in-between ($(2.3 \pm 0.1) \times 10^{-12}$ m^2, Figure 2H,I). The differences of these two parameters in different directions were in accordance with the nature of anisotropic structures. Measurement of these scaffold characteristics enables the accurate simulation of oxygen transport.

An ideal channel network that mimics blood vessels in native tissues/organs is generally regarded as the most efficient for oxygen and nutrient transport.[18] However, due to the limited resolution of μCT scanning and manufacturing difficulty, it is rather challenging to fully replicate blood vessel geometry with defined features down to several micrometers. Moreover, the fully replicated vascular geometry might not be mandatory for many in vitro scenarios where cell density within a 3D scaffold (10^6–10^7 cells cm^{-3}) has been widely reported to be much lower than that of native tissues ($\approx 10^8$ cells cm^{-3}).[19] As an alternative design method, fractal design has been extensively employed as a biomimetic channel network design for efficient oxygen transport in isotropic structures.[19] In fact, fractal design is also widely found in native tissues and organs including the human

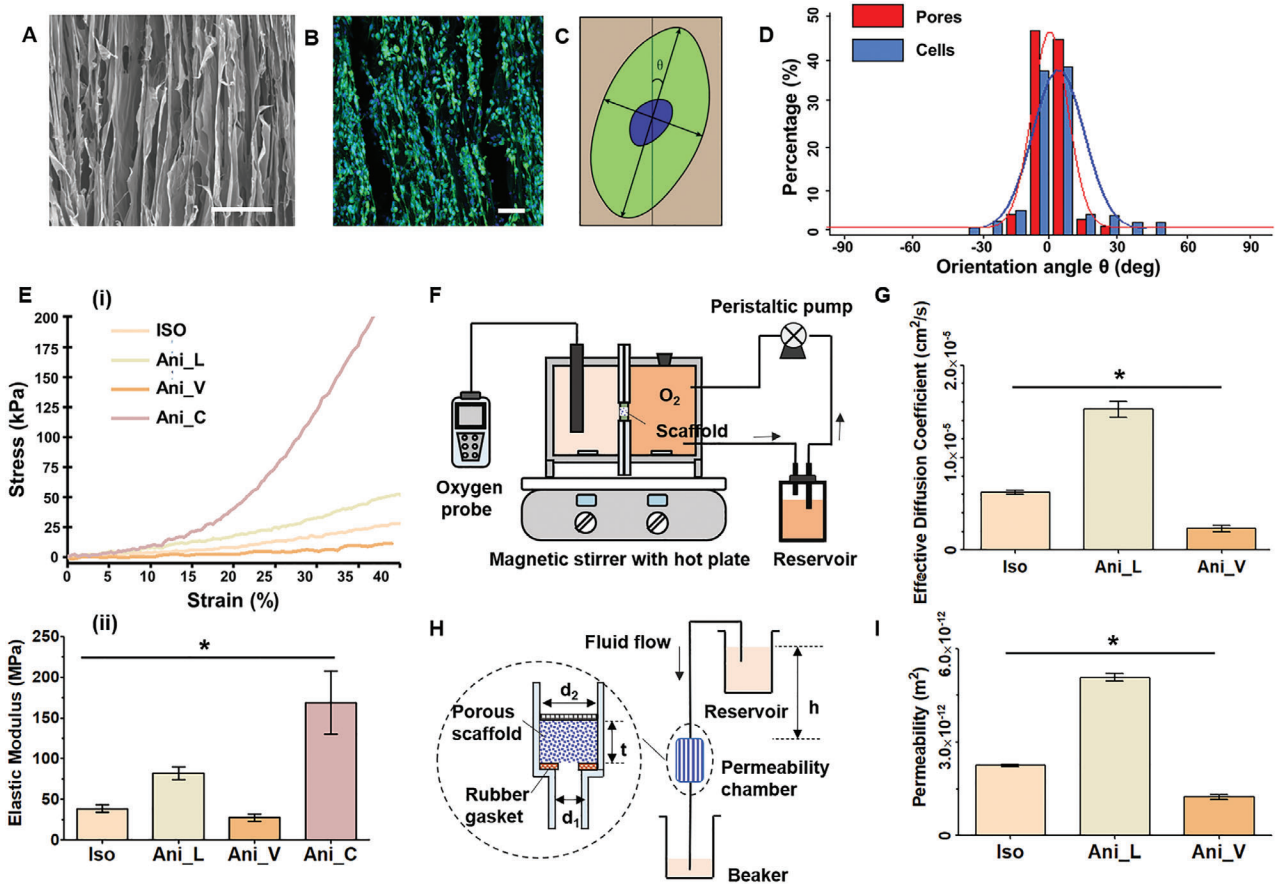

Figure 2. Characterization of fabricated scaffold anisotropic properties including cell alignment as well as mechanical and mass transport properties. A) Scaffold cross-section SEM images showing the oriented micropores (scale bar: 200 μm). B) Fluorescence microscope images of C2C12 cells seeded in the scaffold on day 3 showing cell alignment (green for phalloidin, blue for DAPI; scale bar: 100 μm). C) Diagram of cell orientation and the orientation angle. D) Statistical distribution of cell and micropore orientation angles. E,i) Representative uniaxial tensile stress–strain plots and ii) determined elastic moduli of the isotropic (Iso) and anisotropic scaffolds in different directions (Ani_L, Ani_V, Ani_C). Ani_C denotes the Ani_L in the presence of channel network. F) Diagram of the oxygen diffusion measurement apparatus consisting of two chambers separated by the porous scaffolds. G) Comparison of the measured effective oxygen diffusion coefficient of isotropic (Iso) and anisotropic scaffolds in different directions (Ani_L, Ani_V). H) Diagram of experimental setup for measuring hydraulic permeability. I) Comparison of measured hydraulic permeability of isotropic (Iso) and anisotropic scaffolds in different directions (Ani_L, Ani_V). One-way ANOVA and post hoc Bonferroni test were used to analyze the data, $*p < 0.05$.

cardiovascular system (fractal dimension ≈ 2.3), brain (fractal dimension ≈ 2.7), and respiratory system (fractal dimension ≈ 2.17).[20]

The symmetric bifurcation model has been serving as a widely used fractal unit in tissue engineering because of its simplicity and similar flow features to arterial bifurcations.[21] Considering the anisotropic characteristic of the oriented porous scaffold, the symmetric bifurcation model was modified and employed in this study. For each fork, the tilted branch delivered oxygen and nutrients in a new direction and covered more space, while the other parallel branch aligned with the oriented micropores to maintain the structural anisotropy of the scaffold. Generally, the relationship between the diameters of mother and daughter branches in physiology can be described as shown in Equation (1)[4]

$$D_0^{\gamma} = D_1^{\gamma} + D_2^{\gamma} \quad (1)$$

$$\tau_w = \eta \frac{4U}{R_c} \quad (2)$$

where D_0 is the diameter of the mother branch, D_1 and D_2 are the diameters of the daughter branches, γ is exponential index, τ_w is the wall shear stress, η is the culture medium viscosity, U is the average fluid velocity of the culture medium in the channel, and R_c is the channel radius.

As anatomy demonstrates, the γ exponent is mainly determined by the vascular structure and physiological function. Specifically, γ is ≈2 in aortic vessels, 2.5–3 in coronary vessels, ≈2.9 in carotid vessels, and ≈3 in arterioles.[22] When γ is 2, the average flow velocity remains constant due to the conservation of the cross-section areas. When γ is 3, Equation (1), also known as Murray's Law, results in constant wall shear stress as demonstrated in Equation (2).[23] For anisotropic scaffolds, channel network diameters should be higher than those of the oriented micropores (50–150 μm) to provide efficient metabolic transport. Hence, the channel networks resembled native tissue arterioles in terms of diameter (100–1000 μm), resulting in a γ exponent of 3. Therefore, the relationship between the parent and daughter branch diameters of bifurcated channels was determined by

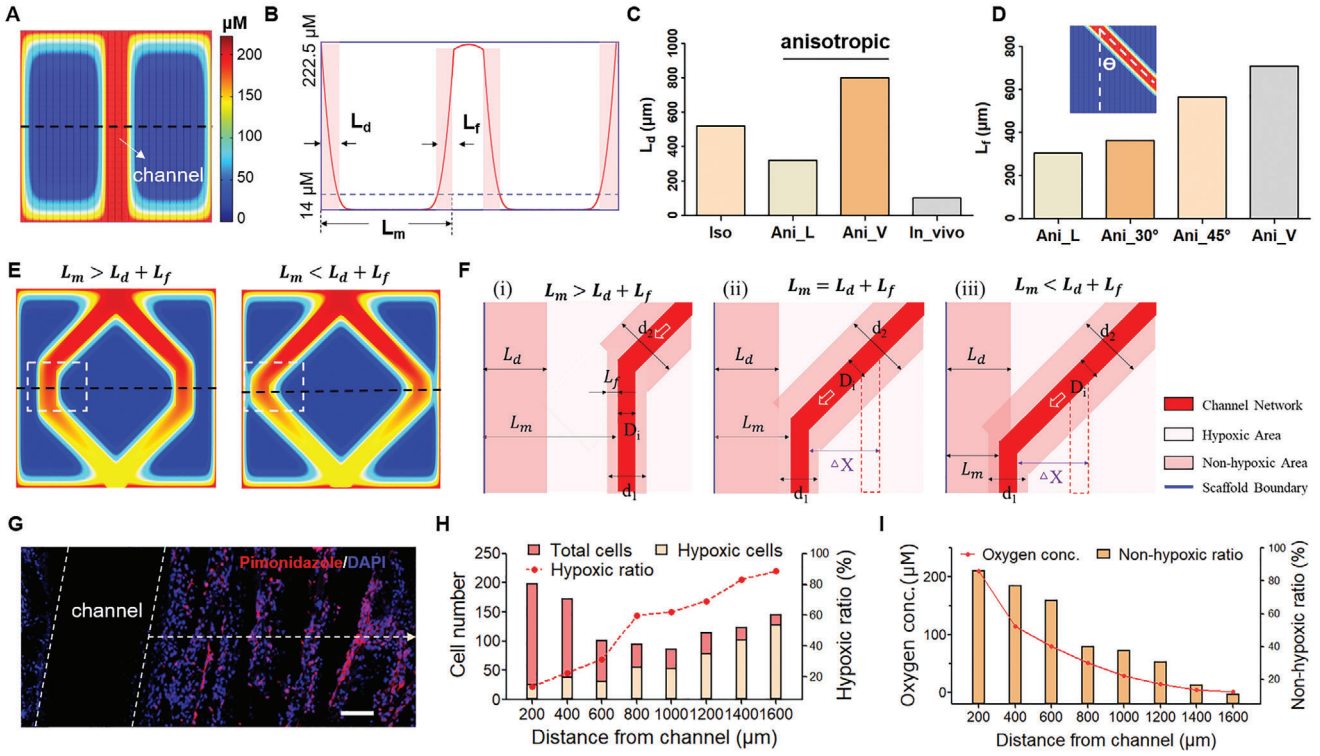

Figure 3. Simulation and validation of oxygen transport. A) Simulated oxygen intensity heatmap of a cell-seeded oriented scaffold with a single channel. B) The effective distance of oxygen transport driven by diffusion (L_d) and flow (L_f). The C) L_d characteristic value and D) L_f characteristic value of isotropic (Iso) and anisotropic scaffolds in different directions (Ani_L, Ani_V). The L_d characteristic value of native tissues (In_vivo) is usually considered to be around 100 μm. E) Simulated oxygen intensity heatmap of a cell-seeded oriented scaffold with a bifurcated channel. F) Illustration of oxygen transport at three different L_m levels compared to the characteristic $L_d + L_f$ value. G) Pimonidazole staining of C2C12 cells (scale bar: 200 μm). H) Hypoxic cell distribution over increasing distances from the channel lumen. I) The relationship between the proportion of nonhypoxic cells and oxygen profiles derived from the simulation.

Murray's Law in this study. Under Murray's Law, wall shear stress remains constant and is accompanied by the lowest global energy loss and flow resistance throughout the vascular system. We further tailored the wall shear stress by tuning the flow velocity and inlet diameters to the physiological range, which is essential for maintaining blood circulation.

An optimal channel network design should ideally possess the capacity to provide oxygen and nutrient delivery to as many cells as possible. It is reasonable to assume that the functional regeneration and maturation of oriented tissues mainly relies on nonhypoxic cells.[24] The number of nonhypoxic cells within the scaffold depends on the cellular oxygen level and total number of cells that can be seeded in the porous zone. Generally, the more branching units the channel has, the more likely a sufficient supply of oxygen and nutrients is able to reach the cells. However, the porous area for cells residing in the scaffold will undoubtedly decrease as more space is occupied by the channels. Channel network designs should be considered inefficient when the increase in nonhypoxic cells is outnumbered by the loss of seeded cells. Therefore, the optimization criterion for channel design is set as the maximum of the nonhypoxic cell numbers or nonhypoxic area ($V_{\text{nonhypoxic}}$) within the scaffold.

The oxygen transport simulation was performed using the measured effective oxygen diffusion coefficient and hydraulic permeability based on the hypothesis that the micropores and cells were uniformly distributed within the anisotropic scaffold. Cell density was assumed to be constant without considering C2C12 cell proliferation; the mathematical model did not consider the influence of HUVECs coverage on the oxygen diffusional permeability. We used Michaelis–Menten kinetics to characterize the oxygen consumption of cells residing in the porous zone as previously reported.[25] Additionally, the oxygen concentrations at the scaffold boundary and channel inlets were set consistent and saturated (222.5×10^{-6} M) at all times for perfusion culture. The simulated oxygen profile of a cell-seeded oriented scaffold with a single channel is shown in **Figure 3**A. Unsurprisingly, the oxygen concentration decreased as the distance from the channel lumen or scaffold boundary increased. Metabolite transport within the scaffold could be divided into two types: static diffusion-driven transport from the scaffold boundary and flow-driven transport within the channels. The effective oxygen transport distance driven by static diffusion (L_d) was defined as the distance between the scaffold boundary and the point at which hypoxia (oxygen concentration $< 14 \times 10^{-6}$ M) first occurred. Similarly, the effective oxygen transport distance driven by flow (L_f) was defined as the distance between the channel lumen and the point at which hypoxia first occurred (Figure 3B). The characteristic L_d and L_f values were calculated from the simulated oxygen profile as shown in Figure 3C,D. For oriented porous scaffolds, the measured L_d value at the Ani_L

direction was much higher than that at the Ani_V direction (800 µm versus 320 µm, respectively). In contrast, the isotropic porous scaffold had a characteristic L_d value between the two oriented scaffold values (520 µm). The effective transport distance of oxygen and nutrients in native tissues is usually considered to be around 100 µm, which is much smaller than that of our scaffolds owing to the distinct porous characteristics.[9] Similarly, for oriented scaffolds, the measured L_f at the Ani_L direction was much smaller than that at the Ani_V direction (302 µm versus 708 µm, respectively). Furthermore, the L_f at 30° and 45° angles to the oriented micropores was 362 µm and 564 µm, respectively. The L_f orientation angle-dependent characteristic was likely due to the anisotropic mass transport properties of the oriented porous scaffold.

According to the equations governing oxygen transport simulation (Equations (3)–(6)), the L_d and L_f characteristic values were mainly determined by the mass transport properties of the scaffolds and the cellular oxygen consumption rate. That is, the characteristic L_d and L_f values were determined by the scaffold pore characteristics, cell type, and cell seeding density. Owing to their independence of the scaffold dimensions, we further used the characteristic L_d and L_f values to guide the optimal channel network design within the scaffolds. For an anisotropic scaffold with a bifurcated channel, the distance between the scaffold boundary and the adjacent channel lumen was defined as L_m, while the distance of two adjacent channels was defined as L_n (Figure 3B). The nonhypoxic area reached the maximum ($L_m = (L_d + L_f)$) at the point where the channel first entered the effective diffusion sphere of the scaffold boundary. The same held true in terms of oxygen transport ($L_n = 2L_f$) when the channel first reached the effective sphere of neighboring channels (Figure 3E,F).

The differences between the theoretical model and experimental results were further evaluated by biological assessment. The scaffolds were seeded with C2C12 cells at the same density (5×10^6 cells cm^{-3}) used in the mathematical models and cultured in a custom-made perfusion bioreactor. LIVE/DEAD staining indicated fewer dead cells near the channels than in the scaffold interior (Figure S5A–D, Supporting Information).[26] Pimonidazole immunostaining was used to map the hypoxic region (oxygen concentration below 14×10^{-6} M) across the scaffold (Figure 3G and Figure S5E,F, Supporting Information); pimonidazole forms stable covalent adducts with thiol groups present in proteins, peptides, and amino acids in hypoxic cells and was further detected using monoclonal antibodies. As the distance from the channel lumen increased, more hypoxic cells were found and stained by the pimonidazole probe (Figure 3H). As a function of the distance from the channel lumen, the proportion of nonhypoxic cells corresponded with the oxygen transport simulation-based oxygen profile (Figure 3I). Thus, the oxygen transport simulation results were validated by pimonidazole immunostaining. The biological experiments demonstrated the reliability of the oxygen transport simulation results using experimentally measured anisotropic characteristics. Acknowledging that the transports of different components would have impact on the functionality of tissues, here we have only focused on the transport of O_2 due to its significance and quantifiable characterization. In the future work, we will consider the transport of the nutrient and CO_2 and develop a monitoring method to improve the numerical model that guides the design and optimization of vascular channels.

Scaffold geometry and cell density generally depend on tissue/organ targeted for regeneration. The bifurcated channels in our anisotropic scaffold were designed with a 3:4 aspect ratio (15 mm width × 20 mm height). Due to the structural anisotropy of the scaffold, the flow-driven effective oxygen transport distance (L_f) increased with the increase of bifurcating angle (θ). Though channels with a larger bifurcating angle cover more space for metabolite delivery, a larger bifurcating angle would diminish the scaffold anisotropy and result in pressure loss. Thus, a bifurcating angle was set in the physiologically relevant range ($\pi/25 \leq \theta \leq \pi/4$) at $\pi/4$ for the optimization design. To achieve a surgical connection to host vasculature in vivo, channel inlet branches should possess the same diameter (D_0) as that of the blood vessel adjoining the implant site; proper length is also important as oxygen transport efficiency decreases with the increase of inlet branch length (L_0). For simplicity, inlet branch diameter and length were set at 1 and 2 mm, respectively. The diameter (D_i) of each branch was determined by Murray's Law. The length (L_i) of each branch was widely reported to be positively related to the diameter, as is often observed in hierarchical blood vessels.[23] For each model, the tilted branch lengths were tuned through further design iterations to avoid branch intersection. To achieve an optimal design, bifurcated channels with increasing levels of bifurcation were generated (**Figure 4**A) until the marginal increment of the nonhypoxic area became negative (Figure 4B).

The hypoxic and nonhypoxic areas in the porous zone were calculated based on the oxygen transport simulation (Figure 4C,D). As channels became more branched, the hypoxic area decreased because of the higher oxygen and nutrient transport efficiency. However, the nonhypoxic area initially increased with the increase of bifurcation levels from 0 to 3, then decreased with the continuous increase of bifurcation levels from 3 to 4, which was due to a lack of porous space for cell growth. Cell proliferation is inhibited to attenuate energy consumption when exposed to hypoxic conditions.[27] The DNA quantification assay was performed to evaluate C2C12 cell proliferation within HUVECs-free scaffolds (Figure 4E). The oxygen transport simulation results were further validated by the DNA quantification assay, which presented the same tendency in cell proliferation as the bifurcation level increased from 0 to 3. Additionally, the wall shear stress was calculated as being uniformly distributed by the finite element method for all models (Figure S6, Supporting Information). The flow rate was tuned to make the wall shear stress fall into the narrow physiological range (1.6–3.3 dyn cm^{-2}) required for in vitro perfusion culture. Taken together, channel network bifurcation was optimized at level 3 with minimal channel diameter of 500 µm.

The case study presented here was performed based on an oriented porous scaffold for muscle tissues as a proof of concept. The channel bifurcation level within the scaffold was optimized to achieve a maximum cell population under nonhypoxic conditions while considering the thrombogenic potential. We proposed the characteristic L_d and L_f values calculated from the oxygen profile in the numerical model to depict the cellular oxygen level within the scaffold. Notably, these simulations and experiments demonstrated the important role that anisotropic structures play in influencing mass transfer within the scaffold. For 3D anisotropic scaffolds fabricated using other techniques, mass transfer properties including the effective oxygen diffusion

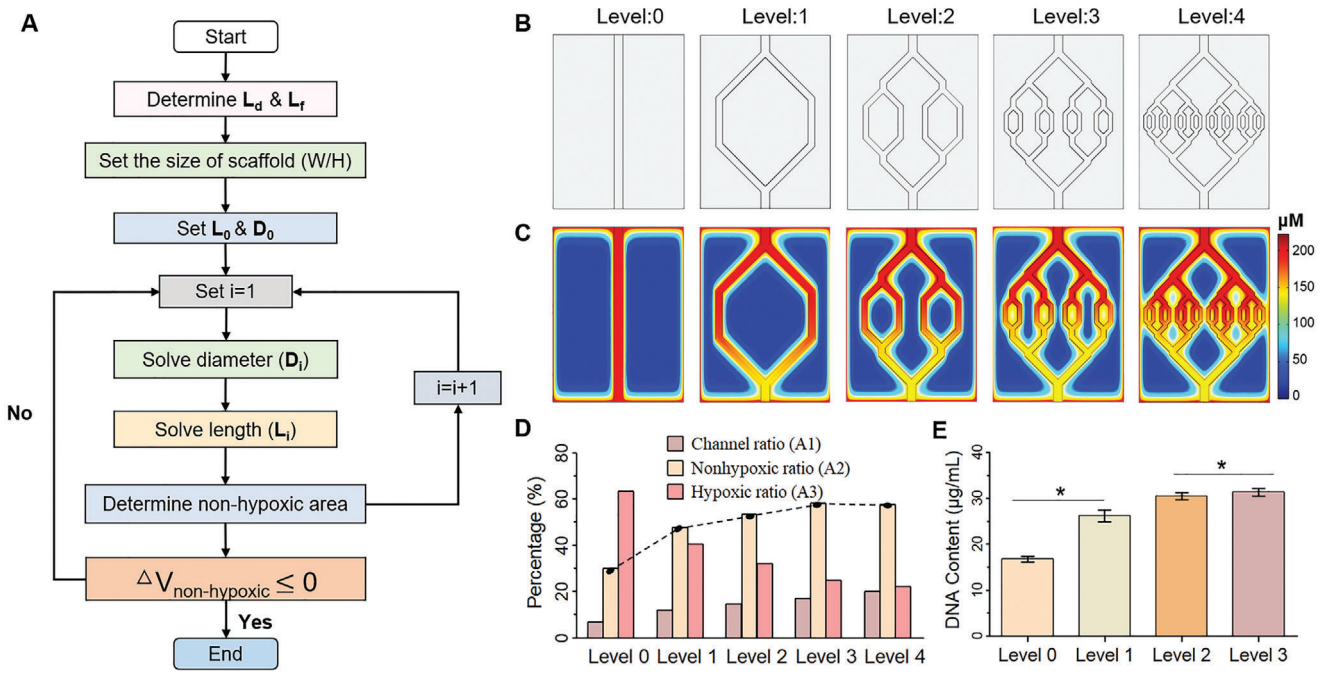

Figure 4. Design and optimization of bifurcated channels within the anisotropic scaffold. A) The flow chart shows the procedure for designing channels within the anisotropic scaffold. B) The geometry of bifurcated channels with bifurcation levels from 0 to 4. C) Simulation of oxygen distribution. D) Analysis of the hypoxic and nonhypoxic areas from the simulation results. E) Changes in cell proliferation evaluated by DNA quantification assay. The DNA content is expressed as μg DNA per mL of the cellular constructs. Student's *t*-test was used to analyze the data, $*p < 0.05$.

coefficient and hydraulic permeability should be experimentally measured and then served as input parameters for our oxygen transport simulation. Moreover, the oxygen consumption rate of specific cell types should be experimentally predefined or referred from related literature for other oriented tissues. Although this study focuses on the single-layer channel structure, the optimized channels in the 2D plane could be readily stacked to achieve multilayer designs within 3D thick tissues. Alternatively, the principles used in this study could be adapted to the design of 3D channels of arbitrary geometry, which however might exhibit more complexity in the geometry of bifurcation (e.g., the asymmetrical ratio of the two daughter branches and the out-of-plane rotation angles). Future work focusing on the development of a 3D vascular tree model is needed.

Despite the increasing interest in fabricating vascular oriented tissues, an approach for designing and optimizing vascular channels within anisotropic scaffolds remains an unmet need. Here, we proposed an effective approach for the fractal design and optimization of bifurcated channels in a cell seeded anisotropic scaffold for oriented tissue engineering. The 3D scaffold integrating channel networks with oriented micropores were successfully fabricated to mimic the vascular and anisotropic structures of oriented tissues, including muscle tissues. The experimentally measured effective oxygen diffusion coefficient and hydraulic permeability served as input parameters for the numerical model. The experiments and oxygen transport simulation presented here highlight the distinct mass transfer within anisotropic scaffolds. Based on an oxygen transport simulation validated by pimonidazole immunostaining and a DNA quantification assay, Murray's Law was used for channel design and optimization. Bifurcation was optimized at level 3 as this level displayed the largest population of nonhypoxic cells. This design strategy performed with a case study for muscle tissues could be further extended to other oriented tissues, which would facilitate the development and application of vascularized oriented tissues.

Experimental Section

Sacrificial Template Fabrication: The sacrificial template was made of PVA (Mowiol 4-88, Sigma-Aldrich, Germany). First, the channel network pattern was designed and converted into standard for the exchange of product model data (STEP) files using AutoCAD Mechanical 2018. The pattern was 3D printed with photopolymer using stereolithography technology and used to cast a PDMS (polydimethylsiloxane) negative mold. PVA solution (20 wt%) was then cast on the PDMS mold and allowed to dry overnight. The PVA structure was carefully removed from the PDMS mold with tweezers. The PVA template was immersed in a solution of PLGA (75:25) in chloroform at a concentration of 5–10 mg mL^{-1} for 5 min to form a thin film on the template surface before use.

Fabrication of Channel-Integrated Anisotropic Scaffold: Scaffolds integrating oriented micropores and channel networks were fabricated as previously described.[9] Collagen (type I from rat tail, Sigma-Aldrich) and chitosan (medium molecular weight, Sigma-Aldrich) were dissolved in aqueous acetic acid solution (1 vol%) to obtain 1 and 1 wt% solutions, respectively. Collagen and chitosan solutions were uniformly mixed and poured into the custom mold with the embedded PVA template. The collagen/chitosan solution was frozen under a unidirectional thermal gradient for 6 h, then freeze-dried (Christ Alpha 1–2 LDPlus, Germany, −45 °C, 0.05 Pa) for 48 h. Then, lyophilized scaffolds were immersed in 0.5 wt% sodium polyphosphate for 30 min to crosslink. The sacrificial structure was dissolved by immersing the scaffolds in deionized water overnight to

generate the channel network. The scaffolds were lyophilized again and stored in a dry environment before use.

Scaffold Morphology: Scaffold morphology was evaluated by SEM. Before observation, the dry samples were sectioned, attached to stubs with conductive resin, and sputtered with gold for 30–60 s. Samples were examined using high-resolution SEM (FEI Quanta 200, Czech Republic) at 0.01 Pa and 20 kV. Scaffold micro CT scanning was performed using a desktop μCT machine (Skyscan 1272, Bruker, Belgium) with a 10 μm pixel size. The 3D scaffold image was reconstructed from the μCT images. The orientation index (OI) was defined to assess the oriented degree of oriented micropores as previously described.[13] Briefly, SEM images at longitudinal section were binarized with Image-Pro-Plus 6.0 software. Angles between each micropores and horizontal line were measured (α_i). The arithmetic mean (α) and deviation angle (β_i) were calculated to obtain the OI value.

Mathematical Model and Oxygen Distribution Simulation: In the channel zone, oxygen transport was assumed to occur via convection and diffusion. Thus, the governing equation for oxygen transport was written as Equation (3)

$$\frac{\partial C}{\partial t} = -(\nabla C \cdot \nu) + \nabla \cdot (D_m \cdot \nabla C) \tag{3}$$

where C was the oxygen concentration, ν and D_m were the velocity of culture medium and the oxygen diffusion coefficient in culture medium, respectively. For fluid dynamics, the incompressible Navier–Stokes model for Newtonian flow (constant viscosity) was used to calculate the velocity field that resulted from convection (Equation (4))

$$\rho_m \cdot \frac{\partial \nu}{\partial t} = -\nabla P - \nu \cdot \nabla \nu + \mu \cdot \nabla^2 \nu + \rho_m \cdot g \tag{4}$$

where μ and ρ_m were the culture medium viscosity and density, respectively. In the porous zone where cells resided, flow characteristics were predicted using the Brinkman equation (Equation (5)) as a model for flow in porous media[28]

$$\rho_m \cdot \frac{\partial \nu_{Bk}}{\partial t} = -\nabla P - \frac{\mu}{K} \cdot \nu_{Bk} + \mu \cdot \nabla^2 \nu_{Bk} + \rho_m \cdot g \tag{5}$$

where ν_{Bk} was the culture medium velocity in the porous zone. Considering the oxygen consumption of cells described by Michaelis–Menten kinetics, the governing equation for the oxygen profile in the porous zone was written as Equation (6)

$$\frac{\partial C}{\partial t} = -(\nabla C \cdot \nu_{Bk}) + \nabla \cdot (D_s \cdot \nabla C) - \rho_c \cdot \frac{V_{O_2\ max} \cdot C}{K_m + C} \tag{6}$$

where D_s was the effective oxygen diffusion coefficient in the scaffold, ρ_c was the cell density, $V_{O_2\ max}$ was the maximum oxygen uptake rate, and K_m was the Michaelis–Menten constant. For the oxygen distribution simulation, a multiphysics model of flow reaction of diluted species in porous media was utilized along with commercial software (COMSOL Multiphysics 5.4). All parameters of the mathematical model are listed in Table S1 in the Supporting Information.

Cell Culture: Human umbilical vein endothelial cells (HUVECs, SV40T antigen transformed HUVEC line) and C2C12 cells were purchased from China Infrastructure of Cell Line Resources in Beijing. Prior to cell seeding, all scaffolds were sterilized overnight under ultraviolet light. Scaffolds were immersed in 75% and 100% ethanol for 2 h each, rinsed three times in sterile phosphate buffered solution (PBS), then wetted in Dulbecco's modified Eagle's medium (DMEM). HUVECs were cultured in DMEM supplemented with 1% nonessential amino acids (NEAA) and 0.01 mg mL^{-1} insulin at 37 °C with a 5% CO_2 atmosphere. Using a syringe pump, 100 μL HUVEC cell suspension containing one million cells was injected into the channel lumen. The cellular constructs were incubated at 37 °C to allow cell adhesion to the channels under static conditions. After 2 h, the scaffold was flipped upside down to facilitate cell adhesion to the other half of the channel. The cellular construct was connected to the perfusion bioreactor at a perfusion rate of 50 μL min^{-1}.

C2C12 cells were cultured in DMEM with 10% fetal bovine serum (Bioind, USA), 1% penicillin/streptomycin (Life Technologies, USA), and 1% minimum essential medium (MEM) NEAA (Life Technologies) and incubated at 37 °C with a 5% CO_2 atmosphere according to American Type Culture Collection protocol. C2C12 cells (5×10^6 cells mL^{-1}) were longitudinally seeded into the anisotropic scaffolds along the direction of micropores by perfusion seeding in addition to pipette seeding on the scaffold surface. After seeding, the cellular constructs were perfused using the custom-made perfusion bioreactor by connecting the channel network via silicon tubing. The perfusion bioreactor was composed of a peristaltic pump, medium reservoir, gas exchanger, and culture chamber. Cell viability within the scaffold was assessed using a live/dead fluorescent assay (Calcein AM/propidium iodide (PI), Life Technologies). Briefly, cellular constructs were washed with PBS and incubated in a solution of Calcein AM and PI for 15–30 min at 37 °C. Live and dead cells were green- and red-labeled, respectively, under a fluorescence microscope.

Pimonidazole Immunostaining: After C2C12s seeding, the cellular constructs were incubated with culture medium mixed with pimonidazole hydrochloride (1:10 000 dilution, Hypoxyprobe, USA). After perfusion culture for 3 d, the C2C12-laden samples were fixed for 30 min in 4% paraformaldehyde solution, frozen, then embedded in an optimal cutting temperature (OCT) compound-embedding medium (Tissue-Tek, Sakura Fineteck Inc., USA). Sections (10 μm) were prepared by cutting the entire frozen scaffold with a cryostat (Leica, Germany). The slices were permeabilized with 0.1% Triton X-100, followed by blocking with 10% bovine serum albumin (Calbiochem, USA) for 1 h at room temperature. The slices were further incubated with RED 594 dye-conjugated antipimonidazole mouse monoclonal antibody (1:50 dilution, Hypoxyprobe, USA) at 4 °C for 1 h, followed by counterstaining with 4',6-diamidino-2-phenylindole (DAPI) for 15 min. Confocal microscopy was performed using an inverted Zeiss LSM 880 (Zeiss, Germany).

Statistical Analysis: All statistical data were collected from at least three parallel samples and expressed as the mean ± standard deviation. Statistical analysis was performed using Graph Pad Prism software (version 6.0) for Windows. Student's *t*-test was conducted for comparison between two experimental groups. Multiple comparisons among three independent groups were performed with one-way analysis of variance (ANOVA) followed by post hoc Bonferroni tests. The values of (*) $p < 0.05$ was considered statistically significant, and (**) $p < 0.01$ was considered highly significant.

Supporting Information

Supporting Information is available from the Wiley Online Library or from the author.

Acknowledgements

This article was written through contributions from all of the authors. The authors greatly acknowledge the funding supports from National Key Research and Development Program of China (2018YFA0703004) and National Natural Science Foundation of China (NSFC, No. 31771108).

Conflict of Interest

The authors declare no conflict of interest.

Keywords

biomimetic designs, channel networks, muscle tissue engineering, scaffolds, vascularization

Received: May 9, 2020
Revised: July 20, 2020
Published online:

[1] a) A. Dewle, N. Pathak, P. Rakshasmare, A. Srivastava, *ACS Biomater. Sci. Eng.* **2020**, *6*, 779; b) K. Sheets, J. Wang, S. Meehan, P. Sharma, C. Ng, M. Khan, B. Koons, B. Behkam, A. S. Nain, *J. Biomater. Tissue Eng.* **2013**, *3*, 355; c) Y. H. Li, G. Y. Huang, X. H. Zhang, L. Wang, Y. A. Du, T. J. Lu, F. Xu, *Biotechnol. Adv.* **2014**, *32*, 347.

[2] a) S. M. Somers, N. Y. Zhang, J. B. F. Morrissette-McAlmon, K. Tran, H. Mao, W. L. Grayson, *Acta Biomater.* **2019**, *94*, 232; b) Z. Shen, S. Guo, D. Ye, J. Chen, C. Kang, S. Qiu, D. Lu, Q. Li, K. Xu, J. Lv, Y. Zhu, *BioMed. Res. Int.* **2013**, *2013*, 146953; c) O. Syed, J. Kim, Z. Keskin-Erdogan, R. M. Day, A. El-Fiqi, H. Kim, J. C. Knowles, *Acta Biomater.* **2019**, *99*, 181.

[3] a) L. Ouyang, J. A. Burdick, W. Sun, *ACS Appl. Mater. Interfaces* **2017**, *10*, 12424; b) Q. Lei, J. He, D. Li, *Nanoscale* **2019**, *11*, 15195.

[4] a) M. Gluais, J. Clouet, M. Fusellier, C. Decante, C. Moraru, M. Dutilleul, J. Veziers, J. Lesoeur, D. Dumas, J. Abadie, A. Hamel, E. Bord, S. Y. Chew, J. Guicheux, C. Le Visage, *Biomaterials* **2019**, *205*, 81; b) R. Wang, X. Yao, T. Li, X. Li, M. Jin, Y. Ni, W. Yuan, X. Xie, L. Lu, M. Li, *Adv. Healthcare Mater.* **2019**, *8*, 1900967.

[5] a) G. C. Engelmayr, M. Y. Cheng, C. J. Bettinger, J. T. Borenstein, R. Langer, L. E. Freed, *Nat. Mater.* **2008**, *7*, 1003; b) W. Lin, W. Lan, Y. Wu, D. Zhao, Y. Wang, X. He, J. Li, Z. Li, F. Luo, H. Tan, Q. Fu, *Regener. Biomater.* **2019**, *7*, 19.

[6] a) A. Tocchio, M. Tamplenizza, F. Martello, I. Gerges, E. Rossi, S. Argentiere, S. Rodighiero, W. Zhao, P. Milani, C. Lenardi, *Biomaterials* **2015**, *45*, 124; b) M. Farina, J. F. Alexander, U. Thekkedath, M. Ferrari, A. Grattoni, *Adv. Drug Delivery Rev.* **2019**, *139*, 92.

[7] D. B. Kolesky, K. A. Homan, M. A. Skylar-Scott, J. A. Lewis, *Proc. Natl. Acad. Sci. U. S. A.* **2016**, *113*, 3179.

[8] J. He, Y. Wang, Y. Liu, D. Li, Z. Jin, *Biofabrication* **2013**, *5*, 25002.

[9] Y. Fang, T. Zhang, L. Zhang, W. Gong, W. Sun, *Biofabrication* **2019**, *11*, 35004.

[10] D. M. Hoganson, H. I. Pryor, I. D. Spool, O. H. Burns, J. R. Gilmore, J. P. Vacanti, *Tissue Eng., Part A* **2010**, *16*, 1469.

[11] N. W. Choi, M. Cabodi, B. Held, J. P. Gleghorn, L. J. Bonassar, A. D. Stroock, *Nat. Mater.* **2007**, *6*, 908.

[12] L. Ouyang, J. P. K. Armstrong, Q. Chen, Y. Lin, M. M. Stevens, *Adv. Funct. Mater.* **2020**, *30*, 1908349.

[13] T. Zhang, L. Jin, Y. Fang, F. Lin, W. Sun, Z. Xiong, *J. Biomater. Tissue Eng.* **2014**, *4*, 1030.

[14] D. B. Kolesky, R. L. Truby, A. S. Gladman, T. A. Busbee, K. A. Homan, J. A. Lewis, *Adv. Mater.* **2014**, *26*, 3124.

[15] K. Ronaldson-Bouchard, S. P. Ma, K. Yeager, T. Chen, L. Song, D. Sirabella, K. Morikawa, D. Teles, M. Yazawa, G. Vunjak-Novakovic, *Nature* **2018**, *556*, 239.

[16] S. Chen, T. Nakamoto, N. Kawazoe, G. Chen, *Biomaterials* **2015**, *73*, 23.

[17] U. Cheema, Z. M. Rong, O. Kirresh, A. J. MacRobert, P. Vadgama, R. A. Brown, *J. Tissue Eng. Regener. Med.* **2012**, *6*, 77.

[18] J. S. Miller, K. R. Stevens, M. T. Yang, B. M. Baker, D. H. Nguyen, D. M. Cohen, E. Toro, A. A. Chen, P. A. Galie, X. Yu, R. Chaturvedi, S. N. Bhatia, C. S. Chen, *Nat. Mater.* **2012**, *11*, 768.

[19] A. Lee, A. R. Hudson, D. J. Shiwarski, J. W. Tashman, T. J. Hinton, S. Yerneni, J. M. Bliley, P. G. Campbell, A. W. Feinberg, *Science* **2019**, *365*, 482.

[20] G. Gao, J. Y. Park, B. S. Kim, J. Jang, D. Cho, *Adv. Healthcare Mater.* **2018**, *7*, e1801102.

[21] J. Khamassi, C. Bierwisch, P. Pelz, *Phys. Rev. E* **2016**, *93*, 62408.

[22] O. Bas, S. Lucarotti, D. D. Angella, N. J. Castro, C. Meinert, F. M. Wunner, E. Rank, G. Vozzi, T. J. Klein, I. Catelas, E. M. De-Juan-Pardo, D. W. Hutmacher, *Chem. Eng. J.* **2018**, *340*, 15.

[23] R. Fan, Y. Sun, J. Wan, *RSC Adv.* **2015**, *5*, 90596.

[24] M. A. Skylar-Scott, S. G. M. Uzel, L. L. Nam, J. H. Ahrens, R. L. Truby, S. Damaraju, J. A. Lewis, *Sci. Adv.* **2019**, *5*, eaww2459.

[25] F. Coletti, S. Macchietto, N. Elvassore, *Ind. Eng. Chem. Res.* **2006**, *45*, 8158.

[26] J. Bussink, J. H. Kaanders, A. J. van der Kogel, *Radiother. Oncol.* **2003**, *67*, 3.

[27] J. W. Lee, G. Ahn, J. Y. Kim, D. W. Cho, *J. Mater. Sci.: Mater. Med.* **2010**, *21*, 3195.

[28] a) F. Mokhtari Jafari, G. Amoabediny, N. Haghighipour, R. Zarghami, A. Saatchi, J. Akbari, N. Salehi Nik, *Eng. Life Sci.* **2016**, *16*, 290; b) T. Kang, J. M. Hong, J. W. Jung, J. J. Yoo, D. W. Cho, *Langmuir* **2013**, *29*, 701.